

# Porphyrin Nanocage-Embedded Single-Molecular Nanoparticles for Cancer Nanotheranostics

Guocan Yu<sup>+</sup>, Tian-Yong Cen<sup>+</sup>, Zhimei He<sup>+</sup>, Shu-Ping Wang, Zhantong Wang, Xin-Wen Ying, Shijun Li,\* Orit Jacobson, Sheng Wang,\* Lei Wang, Li-Sen Lin, Rui Tian, Zijian Zhou, Qianqian Ni, Xiaopeng Li, and Xiaoyuan Chen\*

**Abstract:** Single molecular nanoparticles (SMNPs) integrating imaging and therapeutic capabilities exhibit unparalleled advantages in cancer theranostics, ranging from excellent biocompatibility, high stability, prolonged blood lifetime to abundant tumor accumulation. Herein, we synthesize a sophisticated porphyrin nanocage that is further functionalized with twelve polyethylene glycol arms to prepare SMNPs (**porSMNPs**). The porphyrin nanocage embedded in **porSMNPs** can be utilized as a theranostic platform. PET imaging allows dynamic observation of the bio-distribution of **porSMNPs**, confirming their excellent circulation time and preferential accumulation at the tumor site, which is attributed to the enhanced permeability and retention effect. Moreover, the cage structure significantly promotes the photosensitizing effect of **porSMNs** by inhibiting the  $\pi$ - $\pi$  stacking interactions of the photosensitizers, ablating of the tumors without relapse by taking advantage of photodynamic therapy.

**N**anotheranostics, the nano-enabled combination of therapy and diagnosis, offer promising opportunities in precise diagnosis and effective therapy of cancer.<sup>[1]</sup> Benefiting from their excellent biocompatibility and biodegradability, organic theranostic platforms, especially those fabricated from functional co-polymers, such as micelles, nanoparticles, vesicles, and liposomes, exhibit brilliant promise in the next-gener-

ation theranostics to meet the challenges in cancer management.<sup>[2]</sup> However, one practical challenge impeding the clinical trials of the conventional polymeric nanosystems is their low stability in vivo, arising from the large dilution volume, shearing force, and interactions with biological components in the blood after intravenous injection, which leads to premature release, off-target toxicity, and diminished theranostic performance.<sup>[3]</sup> Additionally, the imaging signals from the nanotheranostic agents hardly reflect the real delivery and excretion behaviors of the loaded therapeutic agents through physical encapsulation because the imaging agents are always conjugated on the polymer backbones, thus making the theranostic results confusing. Therefore, it is urgently desirable to develop single molecular nanoparticles (SMNPs) integrating therapeutic and diagnostic/imaging abilities to solve these issues.

Another fatal obstacle impeding the clinical applications of the chemotherapeutic nanomedicines is the inevitable side effects toward normal tissues. Different from chemotherapy, photodynamic therapy (PDT) as a rapidly developing therapeutic modality can eradicate cancer cells with negligible drug resistance, low side effects, minimal invasion, and less damage to marginal tissues.<sup>[4]</sup> Upon irradiation with light at an appropriate wavelength, the photosensitizer in its excited state interacts with molecular oxygen to generate highly reactive singlet oxygen (<sup>1</sup>O<sub>2</sub>), a cytotoxic species that causes necrosis/apoptosis of the cancer cells.<sup>[5]</sup> However, the <sup>1</sup>O<sub>2</sub> generation quantum yield of the commonly used photosensitizers are unsatisfactory owing to their severe aggregation in aqueous solution, thus greatly lowering the PDT efficacy.<sup>[6]</sup> Furthermore, low accumulation efficiency in tumors of the photosensitizers after systemic administration impairs the clinical applications of PDT and raises challenges for the development of suitable pharmaceutical formulations.

Herein, we synthesize porphyrin nanocages through a template-directed strategy and use them to synthesize SMNPs (**porSMNPs**) through post-modification with polyethylene glycol chains. The size of the resultant SMNPs is within the optimal range for the enhanced permeability and retention (EPR) effect, and the dense PEG corona significantly prolongs their circulation time, both of which are favorable for increasing the tumor accumulation of **porSMNPs**. The porphyrin nanocage acting as the theranostic platform can be labeled by radioactive <sup>64</sup>Cu for positron emission tomography (PET) imaging, allowing the monitoring of the delivery, pharmacokinetic behaviors, biodistribution, and excretion of **porSMNPs** in real time. More interestingly, the rigid structure of the porphyrin nanocage signifi-

[\*] Dr. G. Yu,<sup>[†]</sup> Dr. Z. He,<sup>[†]</sup> Dr. Z. Wang, Dr. O. Jacobson, Dr. S. Wang, Dr. L.-S. Lin, Dr. R. Tian, Dr. Z. Zhou, Dr. Q. Ni, Prof. Dr. X. Chen  
 Laboratory of Molecular Imaging and Nanomedicine, National Institute of Biomedical Imaging and Bioengineering, National Institutes of Health  
 Bethesda, MD 20892 (USA)  
 E-mail: sheng.wang@nih.gov  
 shawn.chen@nih.gov

T.-Y. Cen,<sup>[†]</sup> S.-P. Wang, X.-W. Ying, Prof. Dr. S. Li  
 College of Material, Chemistry and Chemical Engineering, Hangzhou Normal University  
 Hangzhou 311121 (P. R. China)  
 E-mail: l\_shijun@hznu.edu.cn

L. Wang, Prof. Dr. X. Li  
 Department of Chemistry, University of South Florida  
 Tampa, FL 33620 (USA)

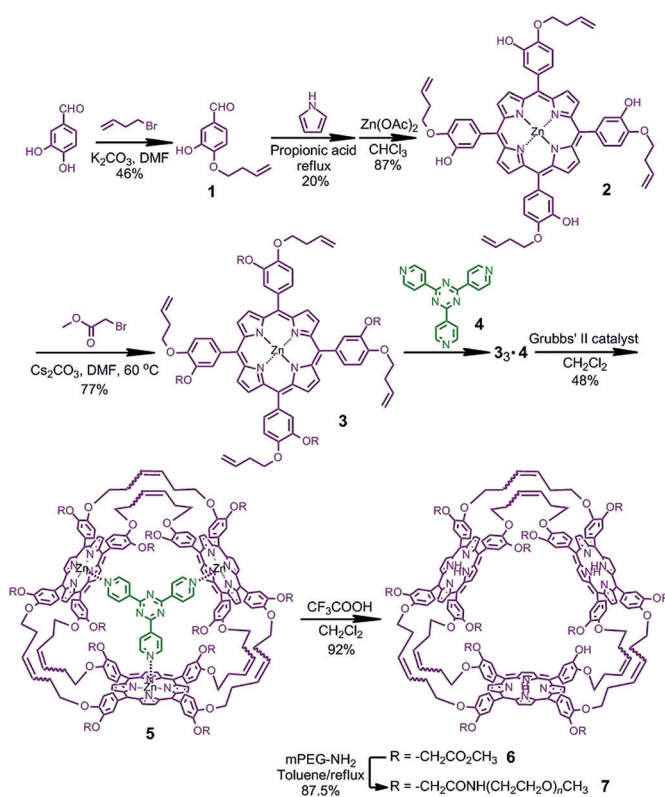
Dr. Z. He<sup>[†]</sup>  
 State Key Laboratory of Analytical Chemistry for Life Science, School of Chemistry and Chemical Engineering, Nanjing University  
 Nanjing 210023 (P. R. China)

[†] These authors contributed equally to this work.

 Supporting information and the ORCID identification number(s) for the author(s) of this article can be found under:  
 <https://doi.org/10.1002/anie.201903277>

cantly inhibits the  $\pi$ - $\pi$  stacking interactions between the photosensitizers, thus boosting the PDT efficacy of **porSMNPs**. Benefiting from the outstanding pharmacokinetic behavior and photosensitizing effect, **porSMNPs** exhibit superior anti-tumor performance, ablating the tumors without recurrence and systemic toxicity, showing unparalleled advantages over a clinically used chemotherapeutic nanomedicine (doxorubicin hydrochloride liposome, Doxil).

The tetraalkene-derived zinc porphyrin derivative **2** was synthesized from the reaction of **1** and pyrrole in propionic acid at reflux for 2 h followed by the coordination with zinc acetate (Scheme 1). After further reaction with methyl bromoacetate, zinc porphyrin monomers **3** were preorganized together to form a triangular-prism trimer **3<sub>3</sub>·4**, in which 2,4,6-tris(pyridin-4-yl)-1,3,5-triazine (**4**) acted as a template. The porphyrin nanocage **5** was prepared through an olefin metathesis reaction using Grubbs II catalyst with a yield of 48%. The template and zinc metals were removed by treating **5** with trifluoroacetic acid. The twelve ester groups were further modified by PEG chains through an amidation reaction by refluxing a mixture of **6** and excessive methoxypolyoxyethylene amine (mPEG-NH<sub>2</sub>, 5 kDa) in toluene. The product **7** was finally obtained by removing the free mPEG-NH<sub>2</sub> using a dialysis bag with a molecular weight cut-off of 50 kDa. Various characterizations including <sup>1</sup>H NMR spectroscopy, <sup>13</sup>C NMR spectroscopy, electrospray ionization mass spectrometry, and gel permeation chromatography (GPC) were performed (Supporting Information, Figure S1–S19). The characteristic peaks related to the protons of the porphyrin



**Scheme 1.** Synthetic route to the porphyrin nanocage-embedded polymer **7**.

nanocage and PEG chains were detected in the spectrum of **7** (Figure S15), indicating the coexistence of these two components. The molecular weight and polydispersity index of **7** were determined to be 69.7 kDa and 1.12 according to the GPC curve (Figure S17), which demonstrated that all of the ester groups were functionalized by the PEG chains.

The solubility of the porphyrin nanocages was significantly improved owing to the PEG chains, more than 500 mg of **7** could be dissolved in water (1 mL) to afford a transparent solution. An intense absorption at 423 nm was observed, related to the typical Soret band, and the Q-bands appeared at 523, 561, 595, and 655 nm in the UV/Vis spectra of **7** (Figure 1a). Excitation of the aqueous solution of **7** at 450 nm gave a strong emission peak at 678 nm (Figure 1a). The fluorescence quantum yield (QY) of **7** was 6.9% in aqueous solution, using tetra-*n*-propylporphycene as a reference (QY = 38%). TEM revealed the morphology and size of **7**. As shown in Figure 1b, spherical nanoparticles with diameters around 20 nm were observed. Dynamic light scattering (DLS) indicated that the average diameter of the PEGylated nanocages was  $34.6 \pm 1.8$  nm (Figure 1b), bigger than the size observed in the TEM image, which was attributed to the existence of a low-contrast flexible PEG layer on the nanoparticle surface as well as the swelling effect in aqueous solution. During the experiments, we noticed that the size of the nanoparticles did not change when gradually diluting the solution, which indicated that no dissociation occurred. Considering the sterically hindered PEG chains on the porphyrin platform, the nanoparticles formed by **7** are SMNPs. Importantly, the **porSMNPs** exhibited high stability in a physiology environment, negligible changes in diameter were detected by DLS in PBS containing fetal bovine serum (10%) over 72 h (Figure S20).

The excellent biocompatibility of **porSMNPs** was confirmed by 3-(4',5'-dimethylthiazol-2'-yl)-2,5-diphenyl tetrazolium bromide (MTT) assay using U87MG cell line. The relative cell viability remained higher than 90% in dark when the concentration of **porSMNPs** reached  $0.64 \text{ mg mL}^{-1}$  (Figure S22). Additionally, the in vivo safety of **porSMNPs** was evaluated using a hemolysis assay. Figure S23 demonstrates that **porSMNPs** were not hemolytic, as indicated by the negligible changes in hemolysis percentage in the test concentration range. The cellular internalization of **porSMNPs** was verified by confocal laser scanning microscopy (CLSM). Red fluorescence was observed in the cytoplasm

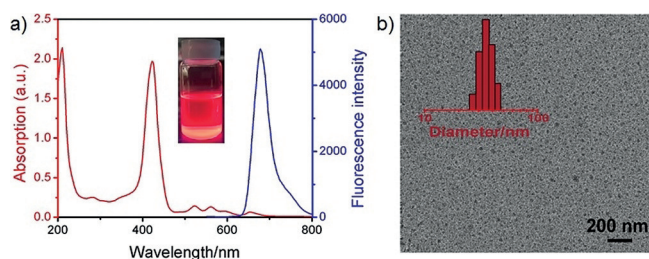


**Figure 1.** a) UV/Vis absorption and fluorescence spectra of **porSMNPs** in aqueous solution. Inset: The **porSMNPs** solution under UV light (365 nm). b) TEM image of the **porSMNPs**. Inset: DLS intensity-weighted size distributions of **porSMNPs** in aqueous solution.

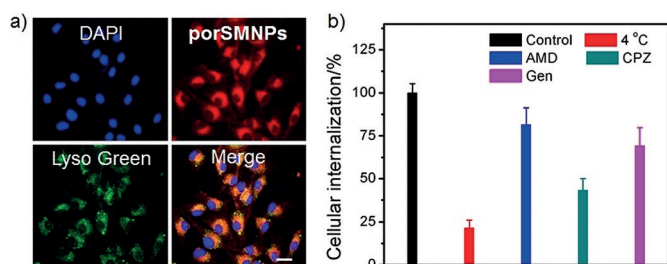


**Figure 2.** a) CLSM images of U87MG cells incubated with porSMNPs for 8 h. Scale bar = 50 μm. b) Probing the mechanisms of cellular internalization by using various inhibitors.

for cells incubated with porSMNPs (Figure 2a). The endocytic pathways of porSMNPs were evaluated using flow cytometry by applying different endocytosis inhibitors. As shown in Figure 2b, the internalization of porSMNPs by the cells was significantly inhibited at 4 °C, suggesting the cellular uptake was energy-dependent. Treatment of the cells with amiloride-HCl (AMD), chlorpromazine (CPZ), or genistein (Gen) led to 18.5%, 56.8%, or 30.7% decrease in the cellular uptake, respectively, indicating the porSMNPs were mainly internalized through a clathrin-mediated endocytic pathway with the assistance of macropinocytosis- and caveolae-mediated endocytosis.

Apart from the enhancement of solubility and biocompatibility, the PEG chains endow the porSMNPs with a stealth character to protect them from being adsorbed by proteins and degraded by enzymes, thus imparting to the PEGylated nanocage a prolonged circulation time.<sup>[7]</sup> In order to investigate the pharmacokinetics and biodistribution of porSMNPs, PET imaging was employed to monitor the

delivery and excretion of porSMNPs by labeling the porphyrin nanocage with <sup>64</sup>Cu through the coordination interactions (Figure 3a). Compared with other diagnostic modalities, PET imaging provides a quantitative readout of the tissue targeting efficiency and pharmacokinetics of the nanotheranostics with deep tissue penetration, highly sensitivity, and non-invasivity.<sup>[8]</sup> Based on thin layer chromatography, the stability of the chelation was 99.2 ± 0.9% even after culturing the <sup>64</sup>Cu@porSMNPs in mouse serum for 24 h (Figure S24), confirming that the PET imaging accurately reported the in vivo behavior of the <sup>64</sup>Cu@porSMNPs rather than the dissociated <sup>64</sup>Cu.

Whole-body PET images were collected at various times post-intravenous (i.v.) injection of <sup>64</sup>Cu@porSMNPs (150 μCi/mouse) into U87MG tumor-bearing mice (Figure 3b). The circulation time of <sup>64</sup>Cu@porSMNPs was roughly calculated to be 11.3 h by monitoring the signal changes in the heart. A quantitative region-of-interest analysis indicated that the <sup>64</sup>Cu@porSMNPs quickly accumulated at the tumor site, 4.1% ID g<sup>-1</sup> (percentage injected dose per gram) uptake was detected at 4 h post-injection, which was further increased to 4.8% ID g<sup>-1</sup> at 24 h post-injection. The signal was maintained at 2.4% ID g<sup>-1</sup> even at 48 h post injection (Figure 3c). Such an efficient tumor localization was attributed to the EPR effect.<sup>[9]</sup> Owing to the capture by the reticuloendothelial system, the radioactive signal in the liver increased from 16.3% ID g<sup>-1</sup> at 1 h post-injection to 20.4% ID g<sup>-1</sup> at 4 h post injection. The excretion of <sup>64</sup>Cu@porSMNPs was also traced using PET imaging. As shown in Figure 3c, the signal in the liver decreased from 23.6% ID g<sup>-1</sup> at 24 h to 18.1% ID g<sup>-1</sup> and 48 h post-injection. Additionally, a high signal in the intestine was observed at 4 h post-injection, while little

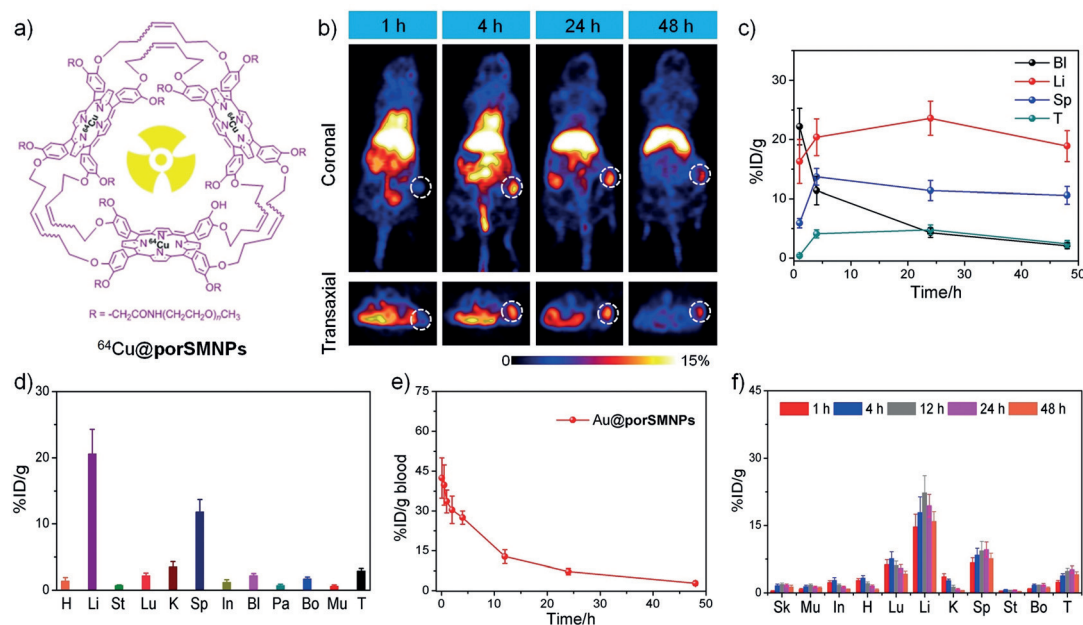


**Figure 3.** a) Radiolabeling of porSMNPs by <sup>64</sup>Cu. b) PET images of the mice bearing U87MG tumor at 1, 4, 24, and 48 h post i.v. injection of <sup>64</sup>Cu@porSMNPs. White circle indicates the location of tumor. c) Time-activity curves of <sup>64</sup>Cu@porSMNPs in the main organs ( $n=3$ ). d) Biodistribution of <sup>64</sup>Cu@porSMNPs in the main organs at 48 h post-injection. e) Plasma concentration versus time after injection of Au@porSMNPs ( $n=4$ ). f) Biodistribution of Au@porSMNPs in the main organs at different time post injection ( $n=4$ ). H = heart, Li = liver, St = stomach, Lu = lung, K = kidney, Sp = spleen, In = intestine, Bl = bladder, Pa = pancreas, Bo = bone, Mu = muscle, T = tumor, and Sk = skin.

radioactivity was detected in the bladder and kidneys, indicating the  $^{64}\text{Cu}@porSMNPs$  was excreted through the hepatobiliary route.

To determine the biodistribution of  $^{64}\text{Cu}@porSMNPs$ , the mice were sacrificed at 48 h post-injection and the radioactivity in different organs was measured through  $\gamma$ -counting, which indicated that the uptake of  $^{64}\text{Cu}@porSMNPs$  by heart, liver, spleen, stomach, kidneys, lung, pancreas, intestine, bladder, bone, muscle, and tumor was  $1.41 \pm 0.32$ ,  $20.6 \pm 3.70$ ,  $11.8 \pm 1.91$ ,  $3.25 \pm 0.47$ ,  $0.73 \pm 0.11$ ,  $2.27 \pm 0.36$ ,  $0.72 \pm 0.16$ ,  $1.17 \pm 0.14$ ,  $2.13 \pm 0.26$ ,  $1.68 \pm 0.25$ ,  $0.56 \pm 0.18$ , and  $2.84 \pm 0.36\%$   $\text{ID g}^{-1}$ , respectively (Figure 2d). Moreover, inductively coupled plasma mass spectrometry was used to verify the accuracy of PET quantification analysis by labeling the porphyrin nanocage with Au. According to Figure 3e, the circulation half-life of  $\text{Au}@porSMNPs$  was  $5.69 \pm 0.36$  h, which was much higher than most of the nanomaterials,<sup>[10]</sup> firmly confirming the prolonged circulation time in blood stream. Time-dependent biodistribution of  $\text{Au}@porSMNPs$  in the main organs also supported the results from PET imaging (Figure 3f).

Excitingly, the cyclic structure of **7** greatly enhanced the photosensitizing effect of **porSMNPs** by inhibiting the  $\pi$ - $\pi$  stacking between the porphyrins. Tetrakis(4-carboxyphenyl)-porphyrin modified with four PEG chains (**TCPPEG**) was utilized as a control. In contrast to **porSMNPs**, **TCPPEG** self-assembled into nanoparticles around 200 nm in diameter, which was attributed to the stacking of the porphyrin core (Figure S25). Singlet-oxygen sensor green (SOSG) was used to trace the generation of  $^1\text{O}_2$ , the characteristic peak at 532 nm increased rapidly upon irradiation in the presence of **porSMNPs** or **TCPPEG** at the same molar concentration of porphyrin photosensitizer (Figure S26). Notably, **porSMNPs** caused a greater enhancement in fluorescence intensity than **TCPPEG** under the same conditions, which demonstrated the photosensitizing effect was boosted by the formation of a confined nanocage (Figures S27 and S28). In sharp contrast with the commercially used photosensitizer (indocyanine green, ICG), **porSMNPs** were highly photostable, negligible changes in fluorescence intensity were detected after several irradiation circles (Figure S29). The intracellular generation of  $^1\text{O}_2$  was shown by dichlorofluorescein diacetate (DCF-DA), a fluorogenic dye that became brightly emissive after being oxidized into DCF. Strong green fluorescence was detected in the cells treated with **porSMNPs** followed by laser irradiation (Figure 4a), evidence of the generation of  $^1\text{O}_2$  inside the cells. Pre-treatment of the cells with vitamin C, a reactive oxygen series scavenger, resulted in the attenuation of the DCF signal, further verifying the successful production of  $^1\text{O}_2$ . An MTT assay indicated that the cytotoxicity against different types of cancer cell lines was activated by laser, and the anticancer efficacy depended on the laser density and irradiation time (Figures S22 and S30–S32). The high phototoxicity index of **porSMNPs** enhanced the therapeutic performance and minimized the side effects.

In vivo anti-tumor studies were conducted. A commercially used chemotherapeutic nanomedicine, Doxil, was employed as a control. When the tumor volume reached circa  $100 \text{ mm}^3$ , the mice were divided randomly and treated

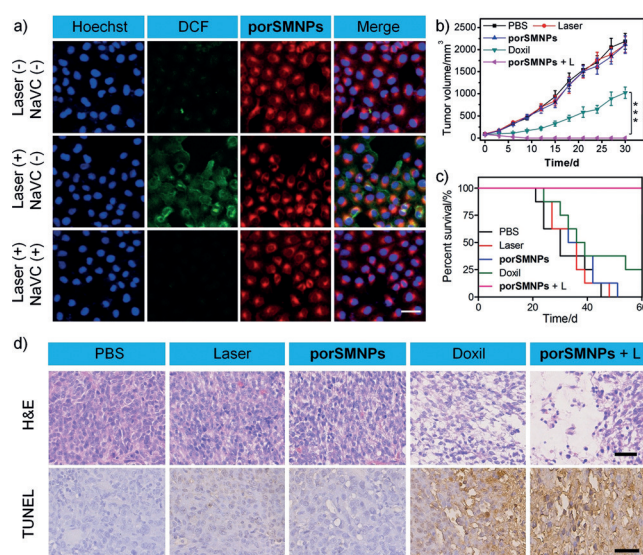


**Figure 4.** a) CLSM images of the cells treated with **porSMNPs** and DCF-DA with/without laser irradiation (671 nm, 0.2  $\text{W cm}^{-2}$ , 5 min) in the absence or presence of vitamin C. Scale bar = 50  $\mu\text{m}$ . b) Tumor growth inhibition curves and c) survival rate of the mice bearing U87MG tumors after different treatments ( $n=8$ ),  $***P < 0.001$ . d) H&E and TUNEL staining of the tumor tissues from the mice treated with different formulations. Scale bar = 200  $\mu\text{m}$ .

with PBS, laser (L), Doxil, **porSMNPs**, and **porSMNPs** plus laser (**porSMNPs + L**). For PDT, the mice only received one laser irradiation (671 nm, 0.1  $\text{W cm}^{-2}$ , 30 min) at 24 h after the first injection, considering the relatively high tumor accumulation of **porSMNPs** at this time point. Compared with the PBS-treated group, limited anti-tumor effect was observed for the mice treated with laser or **porSMNPs** (Figure 4b). Doxil moderately suppressed the tumor growth with an inhibition rate of 53.4% after three injections (Figure S34). However, the tumor relapsed after 12 days because a single chemotherapy round hardly eliminates all cancer cells in tumor sites. Excitingly, **porSMNPs + L** showed superior anti-tumor efficacy, the tumors were completely ablated without recurrence during the treatment period. Transferase-mediated dUTP nick end-labeling (TUNEL) staining indicated that **porSMNPs + L** caused 90.6% cell apoptosis in tumor sites, which was much higher than those of the other formulations (Figure 4d and Figure S35). Hematoxylin and eosin (H&E) staining confirmed that the PDT resulted in the highest level of apoptosis and necrosis in tumor tissues (Figure 4d).

The body-weight loss and survival time of the mice that received different formulations were carefully evaluated. No weight loss was found for the mice treated with **porSMNPs + L** (Figure S37), indicating negligible systemic toxicity of **porSMNPs**. Moreover, no apparent toxic effects were observed during the treatment, including drinking, eating, urination, activity, and neurological status. The median survival time for the mice treated with PBS, laser, **porSMNPs**, and Doxil was 30, 34.5, 36, and 37.5 days, respectively, while the median survival of the mice treated with **porSMNPs + L** was remarkably prolonged over 60 days without a single death (Figure 4c). Urine and blood were collected at different

days during the treatment period for biochemistry assay. The levels of clinical chemistry parameters were all in the normal range compared with the health mice (Figure S38), which demonstrated that no nephrotoxicity and hepatotoxicity were caused by **porSMNPs**. Other vital hematology markers were also in the healthy ranges for the mice treated with **porSMNPs**+L (Figure S39). Unlike chemotherapy with systemic delivery of anticancer drugs, PDT activates the anticancer efficacy locally, thus significantly reducing side effects towards normal tissues.

In conclusion, we synthesized a novel porphyrin nanocage and used it as a platform to prepare SMNPs, which could be applied in cancer theranostics. Different from traditional photosensitizers, the cyclic structure of the nanocage greatly boosted the photosensitizing effect by inhibiting the  $\pi$ - $\pi$  stacking between the porphyrins in aqueous solution, making the **porSMNPs** excellent candidates for PDT. Benefiting from the unique structure and rational modification, prolonged circulation time and high tumor accumulation were achieved, both of which were extremely important for precise diagnosis and effective cancer therapy. In vitro studies demonstrated that **porSMNPs** were highly biocompatible, while their anticancer efficacy was activated specifically by laser irradiation, which was favorable for reducing side effects towards normal tissues. Compared with clinically used Doxil, **porSMNPs** exhibited superior anti-tumor performance, and the tumors were completely ablated by PDT without tumor recurrence. This work provides a theranostic agent with promising potential for clinical translation.

### Acknowledgements

This work was supported by the Intramural Research Program of the National Institute of Biomedical Imaging and Bioengineering, and National Institutes of Health, the National Natural Science Foundation of China (21572042 and 21773052), Zhejiang Provincial Natural Science Foundation of China (LZ16B020002), and the Program for Social Development of Hangzhou (20170533B10). We thank Dr. Vincent Schram at the NICHD Microscopy Imaging Core for technical support.

### Conflict of interest

The authors declare no conflict of interest.

**Keywords:** cancer treatment · imaging · nanotheranostics · photodynamic therapy · singlet oxygen

**How to cite:** *Angew. Chem. Int. Ed.* **2019**, *58*, 8799–8803  
*Angew. Chem.* **2019**, *131*, 8891–8895

- [1] a) K. K. Ng, J. F. Lovell, G. Zheng, *Acc. Chem. Res.* **2011**, *44*, 1105–1113; b) E.-K. Lim, T. Kim, S. Paik, S. Haam, Y.-M. Huh, K. Lee, *Chem. Rev.* **2015**, *115*, 327–394; c) H. Chen, W. Zhang, G. Zhu, J. Xie, X. Chen, *Nat. Rev. Mater.* **2017**, *2*, 17024; d) B. Yu,

H. Wei, Q. He, C. A. Ferreira, C. J. Kuttyreff, D. Ni, Z. T. Rosenkrans, L. Cheng, F. Yu, J. W. Engle, X. L. Lan, W. Cai, *Angew. Chem. Int. Ed.* **2018**, *57*, 218–222; *Angew. Chem.* **2018**, *130*, 224–228.

- [2] a) J. Wu, L. Zhao, X. Xu, N. Bertrand, W. I. Choi, B. Yameen, J. Shi, V. Shah, M. Mulvale, J. L. MacLean, O. C. Farokhzad, *Angew. Chem. Int. Ed.* **2015**, *54*, 9218–9223; *Angew. Chem.* **2015**, *127*, 9350–9355; b) L. Cui, Q. Lin, C. Jin, W. Jiang, H. Huang, L. Ding, N. Muhanna, J. C. Irish, F. Wang, J. Chen, G. Zheng, *ACS Nano* **2015**, *9*, 4484–4495; c) M. H. Lee, A. Sharma, M. J. Chang, J. Lee, S. Son, J. L. Sessler, C. Kang, J. S. Kim, *Chem. Soc. Rev.* **2018**, *47*, 28–52.
- [3] a) M. Elsbahy, G. S. Heo, S. M. Lim, G. R. Sun, K. L. Wooley, *Chem. Rev.* **2015**, *115*, 10967–11011; b) M. Elsbahy, K. L. Wooley, *Acc. Chem. Res.* **2015**, *48*, 1620–1630.
- [4] a) M. Ethirajan, Y. H. Chen, P. Joshi, R. K. Pandey, *Chem. Soc. Rev.* **2011**, *40*, 340–362; b) P. Sun, N. Wang, X. Jin, X. Zhu, *ACS Appl. Mater. Interfaces* **2017**, *9*, 36675–36687; c) S. Goel, C. A. Ferreira, F. Chen, P. A. Ellison, C. M. Siamof, T. E. Barnhart, W. Cai, *Adv. Mater.* **2018**, *30*, 1704367; d) X. Li, N. Kwon, T. Guo, Z. Liu, J. Yoon, *Angew. Chem. Int. Ed.* **2018**, *57*, 11522–11531; *Angew. Chem.* **2018**, *130*, 11694–11704; e) H. Zhu, J. Li, X. Qi, P. Chen, K. Pu, *Nano Lett.* **2018**, *18*, 586–594; f) J. Li, X. Zhen, Y. Lyu, Y. Jiang, J. Huang, K. Pu, *ACS Nano* **2018**, *12*, 8520–8530.
- [5] a) H. Chen, G. D. Wang, Y. J. Chuang, Z. Zhen, X. Chen, P. Biddinger, Z. Hao, F. Liu, B. Shen, Z. Pan, J. Xie, *Nano Lett.* **2015**, *15*, 2249–2256; b) A. Karnkaew, F. Chen, Y. H. Zhan, R. L. Majewski, W. Cai, *ACS Nano* **2016**, *10*, 3918–3935; c) F. Heinemann, J. Karges, G. Gasser, *Acc. Chem. Res.* **2017**, *50*, 2727–2736; d) H. Zhang, K. Liu, S. Li, X. Xin, S. Yuan, G. Ma, X. Yan, *ACS Nano* **2018**, *12*, 8266–8276; e) B. M. Luby, C. D. Walsh, G. Zheng, *Angew. Chem. Int. Ed.* **2019**, *58*, 2558–2569; *Angew. Chem.* **2019**, *131*, 2580–2591; f) J. Li, K. Pu, *Chem. Soc. Rev.* **2019**, *48*, 38–71; g) J. Li, J. Huang, Y. Lyu, J. Huang, Y. Jiang, C. Xie, K. Pu, *J. Am. Chem. Soc.* **2019**, *141*, 4073–4079.
- [6] a) R. Ideta, F. Tasaka, W. D. Jang, N. Nishiyama, G. D. Zhang, A. Harada, Y. Yanagi, Y. Tamaki, T. Aida, K. Kataoka, *Nano Lett.* **2005**, *5*, 2426–2431; b) X. Chen, Y. Li, S. Li, M. Gao, L. Ren, B. Z. Tang, *Adv. Funct. Mater.* **2018**, *28*, 1804362; c) F. Hu, D. Mao, Kenry, X. Cai, W. Wu, D. Kong, B. Liu, *Angew. Chem. Int. Ed.* **2018**, *57*, 10182–10186; *Angew. Chem.* **2018**, *130*, 10339–10343; d) G. Lan, K. Ni, Z. Xu, S. S. Veroneau, Y. Song, W. Lin, *J. Am. Chem. Soc.* **2018**, *140*, 5670–5673.
- [7] K. Knop, R. Hooogenboom, D. Fischer, U. S. Schubert, *Angew. Chem. Int. Ed.* **2010**, *49*, 6288–6308; *Angew. Chem.* **2010**, *122*, 6430–6452.
- [8] a) R. Chakravarty, H. Hong, W. Cai, *Mol. Pharm.* **2014**, *11*, 3777–3797; b) R. Chakravarty, H. F. Valdovinos, F. Chen, C. M. Lewis, P. A. Ellison, H. Luo, M. E. Meyerand, R. J. Nickles, W. Cai, *Adv. Mater.* **2014**, *26*, 5119–5123; c) S. Shi, C. Xu, K. Yang, S. Goel, H. F. Valdovinos, H. Luo, E. B. Ehlerding, C. G. England, L. Cheng, F. Chen, R. J. Nickles, Z. Liu, W. Cai, *Angew. Chem. Int. Ed.* **2017**, *56*, 2889–2892; *Angew. Chem.* **2017**, *129*, 2935–2938.
- [9] a) H. Maeda, H. Nakamura, J. Fang, *Adv. Drug Delivery Rev.* **2013**, *65*, 71–79; b) D. Wang, C. Yu, L. Xu, L. Shi, G. Tong, J. Wu, H. Liu, D. Yan, X. Zhu, *J. Am. Chem. Soc.* **2018**, *140*, 8797–8806.
- [10] M. Yu, J. Zheng, *ACS Nano* **2015**, *9*, 6655–6674.

Manuscript received: March 19, 2019  
Revised manuscript received: April 26, 2019  
Accepted manuscript online: April 29, 2019  
Version of record online: May 23, 2019